Dynamic spreading of re-melted volcanic ash bead on thermal barrier coatings

Shanjie Yang[a,b], Wenjia Song[a,b] *, Yan Lavallee[c], Xin Zhou[b], Donald B. Dingwell[b], Hongbo Guo[a]*

[a] Department of Materials Science and Engineering, Beihang University, 100191 Beijing, China

[b] Department of Earth and Environmental Sciences, Ludwig-Maximilians-Universität München, Theresienstraße 41, 80333 Munich, Germany

[c] Department of Earth, Ocean and Ecological Sciences, University of Liverpool, Liverpool L69 3GP, UK

***Corresponding authors**:

Hongbo Guo, Department of Materials Science and Engineering, Beihang University, Beijing 100191, China. (guo.hongbo@buaa.edu.cn)
Telephone: +86 010 82317117

Wenjia Song, Department of Earth and Environmental Sciences, Ludwig-Maximilians-Universität (LMU), Theresienstrasse 41, 80333 Munich, Germany. (wenjia.song@lmu.de)
Telephone: +49 (0) 89 2180 4293

Abstract

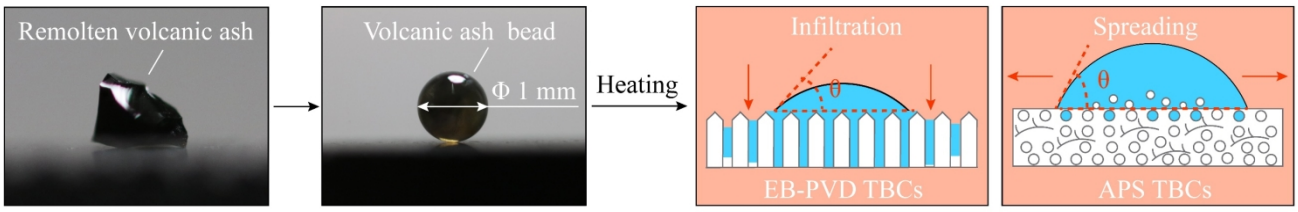

Dynamic spreading of 1 mm diameter volcanic ash bead on thermal barrier coatings (TBCs) surfaces and the infiltration and subsurface lateral flow of these melts within TBCs were quantitatively investigated at 1200-1600 °C for 1-10000 min. The spreading areas, infiltration depths and lateral flow distances are controlled by melt viscosity, coating surface roughness and microstructures. The lateral flow along the inter-column of the coating was dramatically accelerated at higher temperature with a diffusion distance of more than 5.3 mm within 1 min at 1600 °C. These findings are critical for understanding the corrosion mechanism of TBC in contaminated environments.

Key Words: thermal barrier coatings (TBC), volcanic ash, spreading, infiltration, subsurface lateral flow.

1. Introduction

Aviation safety and engine lifespan are routinely threatened by various kinds of atmospheric debris, including volcanic ash, sand and dust [1−7]. Of these, volcanic ash in particular can vary significantly in physical-chemical properties as it commonly consists of both glassy and crystalline phases [8]. The glass transition temperature of the glassy phase in volcanic ash particles (where glass starts to soften and becomes liquid) is at 500~800 °C [9], far below the operating temperature of jet engines (≥ 1200 ºC) [10,11]. Therefore, due to their partially glassy state, volcanic ash particles pose an enhanced threat to aircraft engines compared with other types of siliceous debris as a result of the comparative ease of "liquification" within the engine and the increased risk of TBC-damaging interactions between the resultant silicate melt and interior component surfaces.

When particles of volcanic ash are ingested into jet engines, they typically melt in the combustion chamber (flame temperature ~2000 °C) and adhere to the surfaces of hot interior components (e.g., nozzle guide vanes and high-pressure turbine blades) [12−15]. Those components are typically coated with thermal barrier coatings (TBCs) [16] to improve their resistance to extreme operating conditions.

These TBCs, consist of a ceramic layer with low thermal conductivity and an underlying metallic bond coat, and are designed to protect the underlying components from corrosive gases and particles at operational temperatures (~ 1200-1500 ºC) [17−21]. Currently, industry standard ceramic coatings are made of 7 wt.% Y_2O_3 partially-stabilized ZrO_2 (7YSZ) [22,23]. 7YSZ coatings which typically used in the stationary parts of jet engines are deposited by atmospheric plasma spray (APS) to form a lamellar microstructure with a low thermal conductivity [24,25]. In contrast, the coatings applied to rotating components of aero-turbines (i.e., high-pressure turbine blades), which are subjected to high mechanical loading, are fabricated by electron-beam physical vapour deposition (EB-PVD) to create a columnar microstructure with an enhanced tolerance to thermal stresses [26].

As operating temperatures of jet engines are increased in an effort to improve engine efficiency, the threat that low-viscosity molten volcanic ash poses to TBCs is increased. Such molten silicate

deposits can physically wet, spread over, infiltrate into, and chemically interact with these TBCs leading to their premature degradation [27,28]. When TBCs fail, the underlying engine components are exposed to corrosive gases and extreme temperatures, which may ultimately result in catastrophic failure [29].

Significant efforts have been devoted to studying both the chemical reactions [30−36] and the mechanical damage [37−40] in TBCs caused by volcanic ash [41]. Yet, the mechanisms of wetting and spreading which throughout the whole degradation procedure and largely dictate the extent of resulting degradation (range and depth of chemical interactions and mechanical damage) on TBCs, have not been clearly elucidated [42].

Here, different from the common method of evenly covering TBCs with CMAS, we explore the spreading and infiltration dynamics of glassy volcanic ash beads of 1 mm in diameter on APS and EB-PVD TBCs over a wide range of temperatures and dwell times. By standardizing the mass and the size of the glass beads, interaction parameters (spreading radius, vertical infiltration depth and lateral flow distance) of each test group are rendered comparable. The spreading and infiltration behaviour between the melts and coatings has been documented post-experiment in order to elucidate the underlying mechanisms of interaction and degradation.

2. Experimental

2.1 Chemical analysis and viscosity measurement of volcanic ash

A volcanic ash sample (14TUN05) from the February 2014 explosive eruption of Tungurahua Volcano, Ecuador (Fig. 1a), was chosen for this study [43]. Major element compositions, expressed as oxides, were determined using X-ray fluorescence (XRF) spectroscopy. The geochemical analysis reveals that the ash is dacitic, with a SiO_2 content of 58.12 wt.% SiO_2 (Figs. 1b and c).

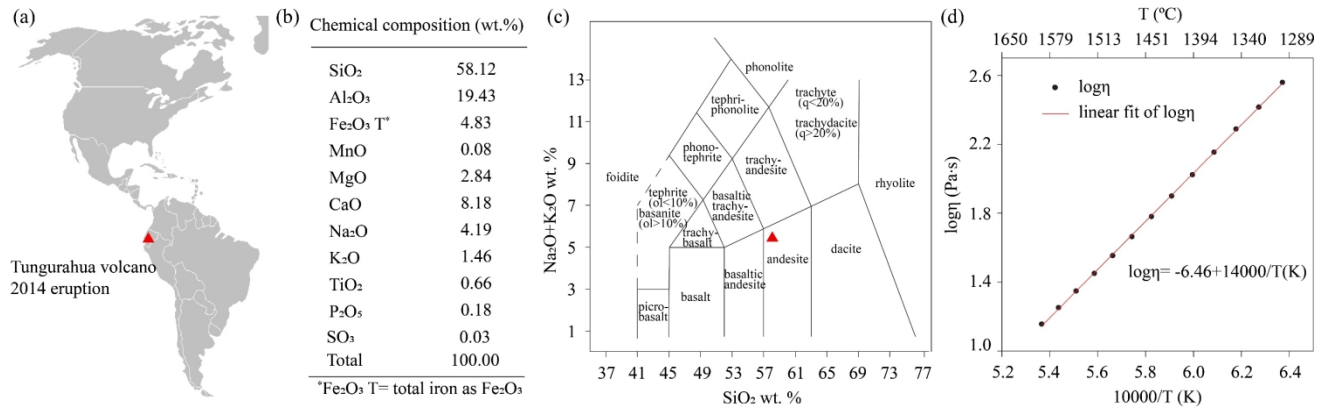

Fig. 1. Physical and chemical properties of Tungurahua volcanic ash. (**a**) Geographic location of the volcano. (**b**) Chemical composition of the ash. (**c**) Geochemical classification based on the total alkali-silica plot. (**d**) Viscosity-temperature relationship with regression (The viscosity data are listed in Table S1).

The viscosity of a Tungurahua volcanic ash melt was determined using a concentric cylinder viscometer at Ludwig-Maximilians-Universität München (The details on viscosity measurement are shown in the Supplementary Method: Viscosity measurement of Tungurahua volcanic ash and Fig. 1d) [44]. Note that the lowest temperature value (1297 °C) in Fig. 1d represents the liquidus temperature, below which melt crystallization may begin. The glass transition temperature of the Tungurahua volcanic ash was estimated based on the Giordano et al. (GRD) model (Tg=718 °C) [45,46].

2.2 Preparation of re-melted volcanic ash glass beads

In order to eliminate any interference effects due to the presence of crystals in volcanic ash, an initial high temperature homogenisation was performed. Approximately 100 g of volcanic ash were heated to 1600 ºC in a platinum crucible in order to completely re-melt the material (Fig. 2a) followed by quenching of the sample in air. In order to generate spherical volcanic ash beads (referred to below simply as "beads") with the diameter of 1 mm, the quenched melts were crushed into small fragments (Fig. 2b) and the glass density (2.781 g cm^{-3}) was measured using an automatic

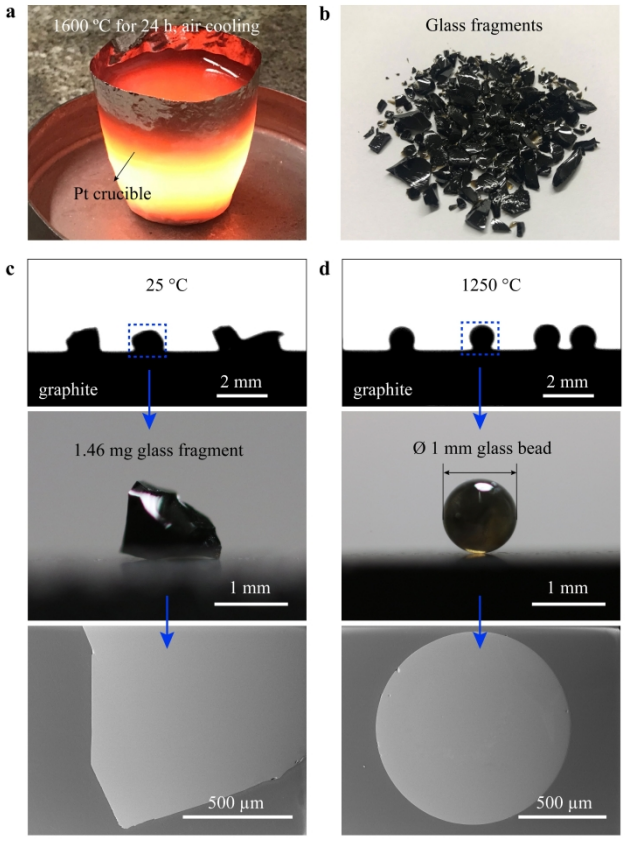

Fig. 2. Re-melted Tungurahua volcanic ash glass beads preparation. (**a**) Tungurahua volcanic ash heated, annealed and homogenized at 1600 °C in a platinum (Pt) crucible. (**b**) Fragments of re-melted volcanic ash glass formed by crushing the quenched material produced in Fig. 1a. (**c**) Profile photo (above), macrograph (middle) and SEM image (below) of selected fragments with masses of 1.46 mg. (**d**) Profile photo (above), macrograph (middle) and SEM image (below) of 1 mm re-melted volcanic ash glass bead created by heating glass fragments at 1250 ºC for 1 hour in vacuum (< 10^{-3} Pa) on a graphite substrate.

density analyzer (Quantachrome instruments, ULTRAPYC 1200e, America) in order to enable the calculation of the mass of material required to produce a sphere of the desired size (i.e, 1.456 mg Fig. 2c). Graphite is a highly melt-phobic material at high temperatures (1100-1400°C) and in the absence of oxygen, with the result that melt droplets do not wet graphite surfaces and yield droplet with a contact angle greater than 150° [47]. In this manner, a spherical bead was created by melting a 1.456 mg fragment on a graphite substrate. Here, the fragment and graphite substrate assembly was fixed in an optical contact angle measuring system (Dataphysics, OCA 25-HTV 1800, Germany) which quantifies the evolution of wetting during heating to 1300 °C in vacuum (heating rate of 5 °C min^{-1}, vacuum conditions < 10^{-3} Pa). The sample was held at 1300°C for 1 hour after which the glass fragment had transformed into a spherical drop (Fig. 2d) with a roundness of 0.836 (calculation of

roundness is described in Fig. S1). The melt droplets so produced were then cooled down in the furnace.

Using a scanning electron microscope (SEM, HITACHI SU5000, Japan; parameters described in Fig. S2), the prepared fragments (Fig. 2c below) and beads (Fig. 2d below) were confirmed to be physically homogeneous, lacking crystals or bubbles. Thus, we infer that the liquidus temperature (at which the material is completely molten) of the re-melted material is below 1300 °C.

2.3 Preparation and characterization of TBCs

Standard 7YSZ coating were deposited on Al_2O_3 substrates (Purity≥99.7 %, 14×10×3 mm, Hesse Instruments, Germany) by APS (Oerlikon Metco 7M, Switzerland) and EB-PVD (Paton UE-205, Ukraine), respectively. The processing parameters for APS and EB-PVD thermal barrier coatings are listed in Table 1.

Table 1 Processing parameters for Thermal barrier coatings

APS TBCs		EB-PVD TBCs	
Power (kW)	41	Power (kW)	43
Spray distance (mm)	85	Rotation speed (rpm)	20
Carrier gas Ar (slpm*)	7	Deposition pressure (Pa)	8×10^{-3}-2×10^{-2}
Plasma gas Ar/H_2 (slpm)	35/12	Substrate temperature (°C)	900
Feed rate (g/min)	20	Deposition rate (μm/min)	~5

*slpm: standard liter per min.

The surface roughness of the TBCs was measured using a confocal laser scanning microscope (Olympus, LEXT OLS4100, Japan) equipped with 2D/3D form measurements, with vertical and horizontal resolution limits of 8 and 120 nm, respectively.

The microstructures of the TBCs are shown in Fig. 3. The as-sprayed APS coating reveals a typical lamellar structure which contains an amount of unmelted particles (marked in Fig. 3a with an arrow). Such unmelted particles are main constituent of the porosity of APS TBCs, beneficial to low thermal conductivity. The thickness of the APS TBCs is ~250 μm (±15 μm) and the porosity was measured to be ~22% by using Image J software. The EB-PVD TBCs (Fig. 3b) reveals a typical columnar structure with a thickness of ~205 μm (±10 μm) and a porosity of 15%. The difference in thickness

between two kinds of TBCs are related to the preparation processes. The 3D surface roughness Sa, i.e. the arithmetical mean height, of APS TBCs (Sa= 9.87 μm) is higher than that of EB-PVD TBCs (Sa= 5.42 μm).

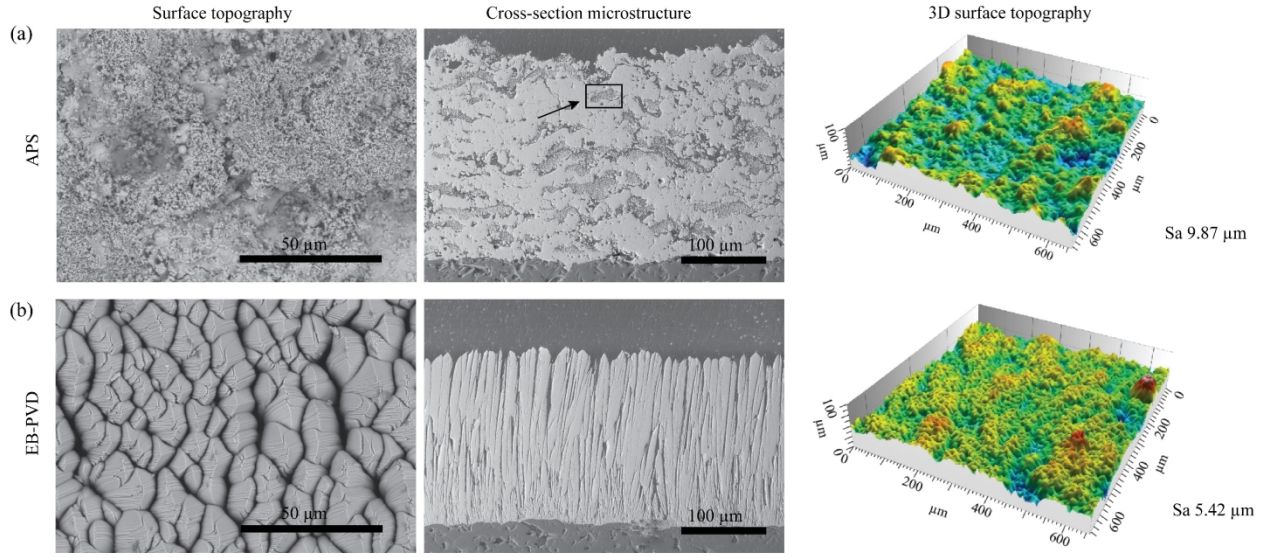

Fig. 3. Surface morphologies, cross-sectional microstructures and the 3D surface roughness of the initial TBCs. (**a**) APS TBCs (the black arrow marked the inclusion in APS TBCs). (**b**) EB-PVD TBCs.

2.4 Observation of volcanic ash melts spreading and infiltration

Here, in order to simulate the actual thermal trajectory of ash in the engine, each sample assembly (a glass bead on the surface of a TBC, Fig. 4a) was inserted into a muffle furnace and thereby exposed to high temperature at atmospheric pressure (referred to here as thermal shock testing, Fig. 4b). The experimental temperatures in this study were 1200 ºC, 1400 ºC and 1600 ºC, with an exposure time varying from 1 to 10^4 min). After heating, the samples were removed from the furnace and rapidly quenched under atmospheric condition (Fig. 4c).

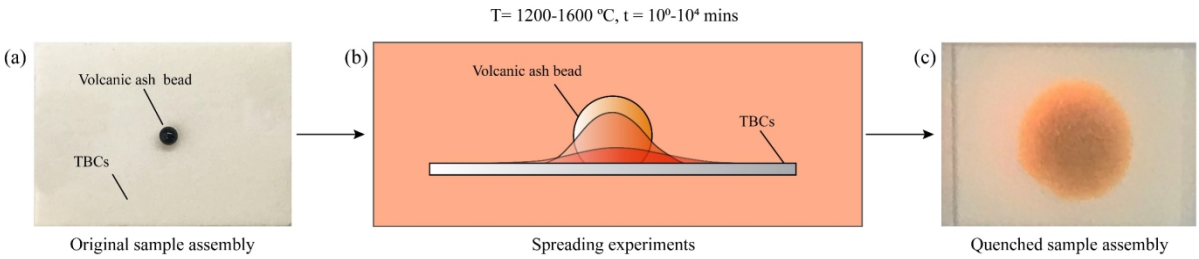

Fig. 4. Sketch of experimental procedure. (**a**) Original sample assembly. (**b**) Spreading experiments. (**c**) Quenched sample assembly.

The spreading areas of the molten beads (referred to as melt) do not describe perfect circles. To eliminate the influence of any anisotropy of the spreading radius, an equivalent average spreading radius (r) was calculated for a perfect circle with equivalent area. Here, a combination of high-resolution imaging and both PhotoShop and ImageJ software was used to confirm and measure the spreading area of the post-experiment samples (Fig. 5).

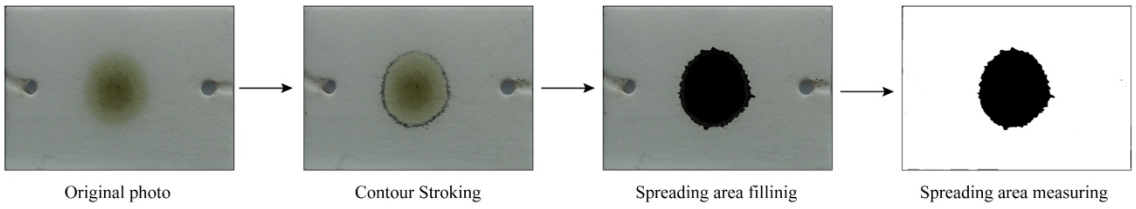

Fig. 5 Measurement of spreading areas.

An SEM equipped with an energy-dispersive X-ray spectrum spectroscopy (EDS) (Oxford Instruments, X-Max^N, United Kingdom) was used to characterize the post-treated surface and cross-sectional morphologies of the samples. Elemental mapping of silicate (Si) by EDS was adopted as a method to describe the depth of Si melt infiltration into the TBCs (parameters of SEM image and Si elemental mapping are described in Fig. S2).

3. Results

3.1 Spreading dynamics of volcanic ash melts on TBCs

In order to observe *in situ* the evolution of melt spreading area on TBCs at different temperatures, the surface macrograph and spreading radius of each sample assembly were measured. The results of the analysis are shown in Fig. 6, and the spreading radius data are listed in Table S2.

The glass beads were stuck to APS and EB-PVD TBCs after being exposed to 1200 °C for 1 min (current temperature reach 824 °C, see the heating profile of the beads in Fig. S3), but detached from the coating during quenching. With increasing temperature and/or time, the melts spreading area increases. The initial state characterized by a smooth melt spreading front (observed for both TBCs at 1200 °C for 10 min or 1400 °C for 1 min in Fig. 6a) changes to a transition state with gradually decreasing darkness from the melts center towards the rough spreading front (Rectangular frame in Fig. 6a). On the surface of the transition state samples, a central thicker darker-colored melt area is surrounded by a thinner lighter-colored area. As the temperature and duration of heating increase, the melts gradually evolved into the final state, where the spreading and infiltration are more severe and the color of the spreading area became lighter (e.g., Fig. 6a on the right-side of the transition state samples). For melts that spread for yet longer dwell times, the spreading front become too light to be detected in this manner and the corresponding spreading radii were thus not measurable ("No data" in Fig. 6a). A buckling spallation occurred on the APS top coating at 1600 °C after 10 min and partial spallation on the EB-PVD coating after 10^3 min at the same temperature (marked with black arrow in Fig. 6a) [48]. Accordingly, no spreading data is available for these two cases either.

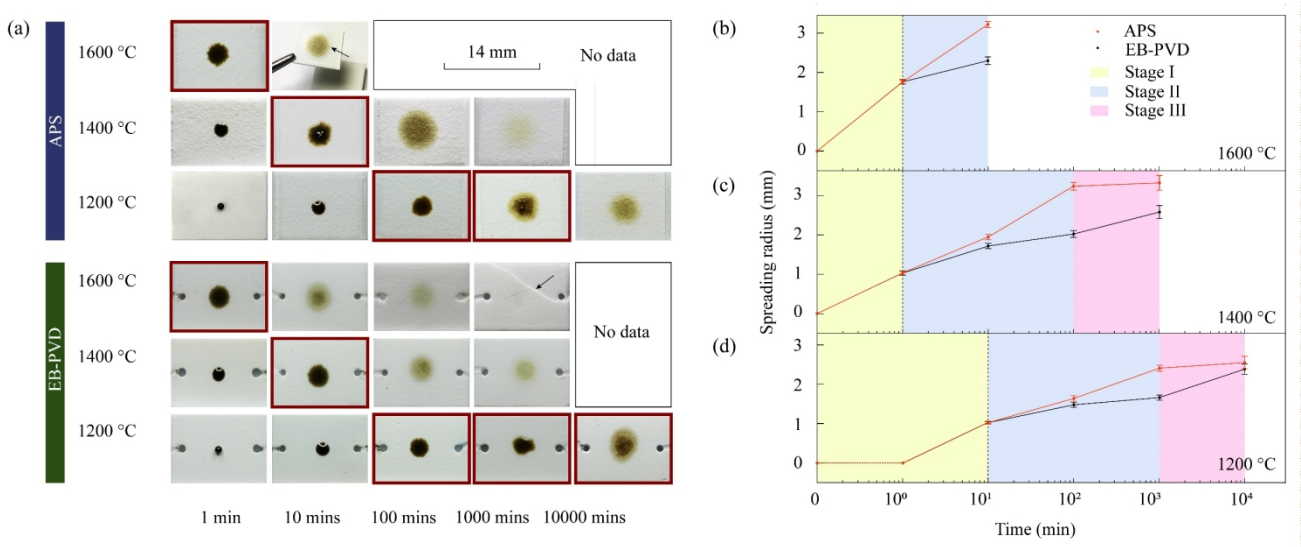

Fig. 6. The spreading behavior of volcanic ash melts on APS and EB-PVD TBCs. (**a**) Photographs of spread samples at 1400-1600 °C for exposure times of 10^0-10^4 min; arrows show spallation. 'No data' indicates where spallation or a spreading front was not detectable; rectangular frames denote samples in the transition state. The graphs at the right side show the average spreading radii (r) as a function of dwell time (t) at a temperature of (**b**) 1200 °C, (**c**) 1400 °C and (**d**) 1600 °C, respectively.

The spreading process of each sample assembly can be divided into three stages (stage I-yellow, stage II-blue and stage III-pink, as shown in Figs. 6b-d) according to the difference of spreading rate $\left({}^{\Delta r}/_{\Delta t}\right)$, that is the slope of the spreading radius (r)-time (t) curve, on APS and EB-PVD TBCs at each temperature. During stage I, at each target temperature, the melt spreading rates on both types of TBCs are similar. Higher temperatures result in a larger spreading area on both TBCs at the end of stage I. In stage II, the spreading rate of the melts on APS TBCs is higher than that on EB-PVD TBCs. This may be attributed to the differing surface roughness and microstructure (lamellar or columnar), which becomes increasingly important as the melt viscosities decrease exponentially as the sample approaching to the target temperature (>362 Pa·s at 1200 °C, 80.7 Pa·s at 1400 °C, 10.3 Pa·s at 1600 °C). In Stage III, the spreading rate of the melts on APS TBCs is lower than on EB-PVD TBCs. This may be due to the higher porosity of the APS TBCs which slows down the spreading after a long period of time. It can be inferred that spallation would occur on the APS coating before stage III at 1600 °C.

As an influence of temperature, the stage I at 1200 °C has longer duration compared to that at 1400 °C, and the starting time point of stage II and stage III at 1400 °C are earlier than that at 1200 °C.

3.2 Infiltration behaviour of re-melted volcanic ash melts on TBCs

Next, we investigated the surface morphology and cross-sectional elemental distributions to explore the influence of melt viscosity, bubbles, surface roughness and microstructure of the coatings on spreading and infiltration during each stages.

To study the influence of melt viscosity on infiltration, the surface and cross-section morphologies of the samples exposed to 1400 °C and 1600 °C for 1 min are compared in Fig. 7. From the surface morphology image taken at the spreading front of the deposited TBCs (Fig. 7a), the melt at 1400 °C has a smooth spreading front compared to that at 1600 °C. The difference is attributed to the temperature dependence of melt viscosity. Lower viscosity melts are influenced by capillary forces to a greater extent [49], and accordingly can flow along the valley of rough surface of TBCs.

Infiltration is a phenomenon that accompanying spreading, and thus in turn affects it. The average infiltration depth was determined from the Si elemental mapping areas, which was measured every 50 μm along the lateral direction, as shown in Fig. 7b, (the summery of infiltration depth are listed in Fig. 8). The infiltration depth increases with temperature in each type of TBCs. For EB-PVD TBCs, the melts infiltration depth reached ~102 μm at 1400 °C, while it was fully infiltrated at 1600 °C after 1 min. For APS TBCs, the infiltration depth reached ~25 μm at 1400 °C and ~84 μm at 1600 °C. We can infer from Fig. 7b that the lamellar structure of APS TBCs has a good infiltration resistance within a short time even when the melt has very low viscosity. The bubbles in the melts on APS TBCs at 1400 °C and 1600 °C (Fig. 7b, marked with arrow) are remarkable, as no bubbles are formed in the melts on EB-PVD TBCs. The formation of the bubbles will be discussed below.

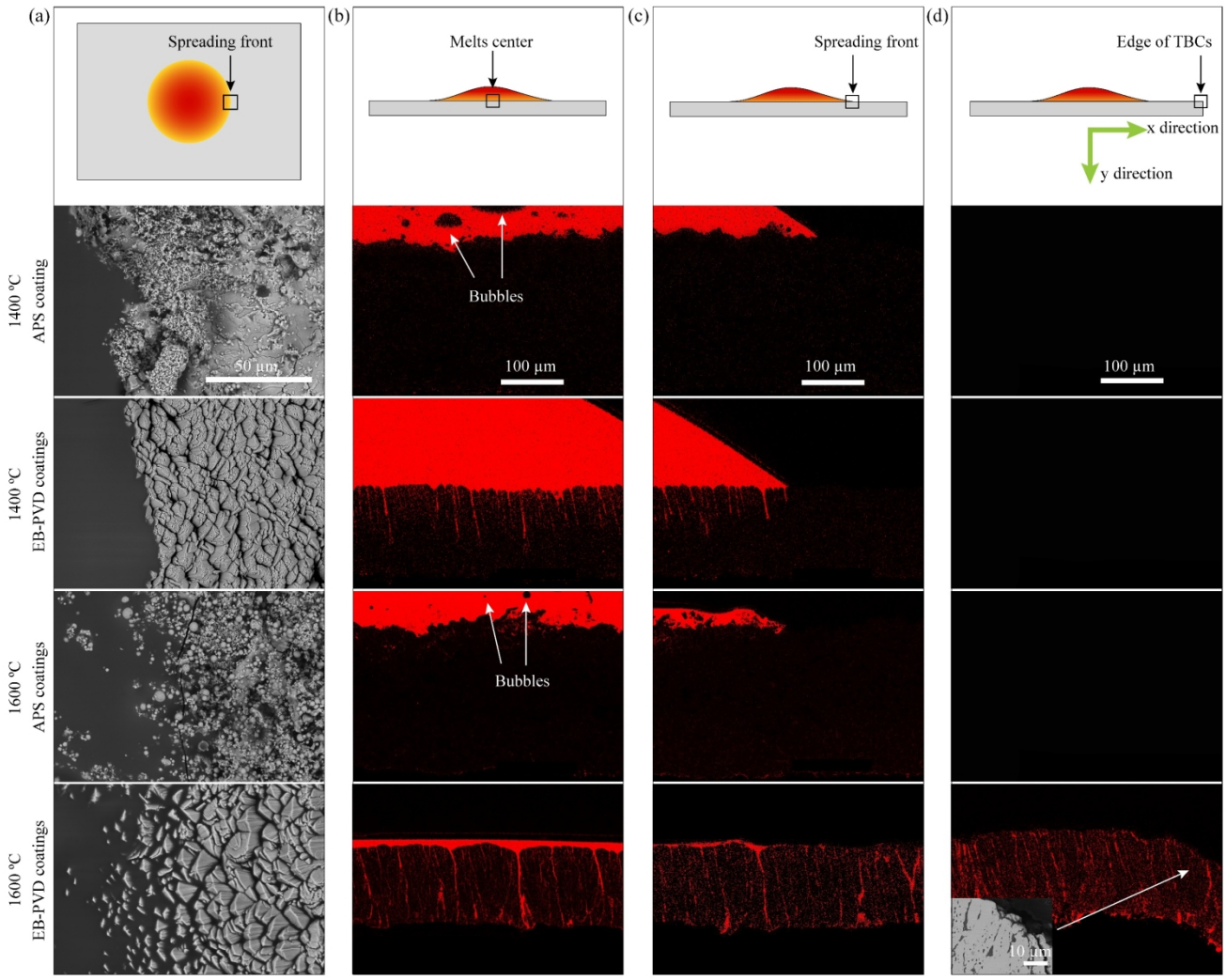

Fig. 7. Surface morphology and cross-section images of the deposited TBCs exposed to 1400 and 1600 °C for 1 min. (**a**) SEM surface morphology images at the spreading front of the deposited TBCs. (**b**) The cross-section Si elemental mapping at the center of melts concentration area. (**c**) The cross-section Si elemental mapping at the spreading front and (**d**) at the edge of the TBC. The SEM image is inserted into the corresponding field of (**d**) to show the microstructure of the infiltrated TBCs.

For the APS TBCs at 1400 °C and 1600 °C, and the EB-PVD TBCs at 1400 °C, only the vertical infiltration occurred under the spread melts (Fig. 7c). For these samples, there is no Si detected below the melt-free zone (Fig. 7d). However, for EB-PVD at 1600 °C, a special phenomenon was observed (Figs. 7c-d bottom): both vertical infiltration and subsurface lateral flow are observed to reach 100% of the scale, that is, the latter even reaches the edge of the TBC sample (diffusion distance >5.3 mm) within 1 min. We can clearly observe obvious sintering caused by silicate melt at the edge of the EB-PVD TBCs (insert in bottom image of Fig. 7d) while no apparent sintering occurs in the melt-free

EB-PVD TBCs (see Fig. S4). In addition, from the surface morphology of Fig. 6a, the edge of the TBCs (EB-PVD at 1600 °C for 1 min) maintains its original color, without evidence of surface contamination, which is further evidence in support of subsurface lateral flow of melt in TBCs. As a result, at high temperature, the contaminated zone can expand rapidly due to the subsurface lateral flow and finally generate a spallation region that exceed the surface spreading area. The lateral flow was also observed to reach the edge of EB-PVD TBCs at 1400 °C after the dwell time of 10 min (see Fig. S5). Therefore, it can be inferred that both the viscosity of the melt and the microstructure of the TBCs are the key factors in influencing subsurface lateral flow. And the lower the melts viscosity, the slower the lateral flow speed.

3.3 Dynamics interplay between spreading and infiltration

In terms of the above experiment phenomena, both dynamics of spreading and infiltration interplay with each other. The temporal evolution of spreading and infiltration was researched by comparing the cross-section SEM images and Si elemental mappings of the two types of TBCs after melt deposition at 1200 °C for 10^1-10^4 min (Fig. 9). The APS sample was fully infiltrated by melt after 10^3 min, while full infiltration occurred on EB-PVD sample within 10^2 min (Figs. 9d and h). The difference in infiltration rate shows that the columnar structure is more easily infiltrated compared to lamellar structure even at 1200 °C when melts has relatively higher viscosity. Combined with the spread rate described in Fig. 6, it indicates that enhanced infiltration reduced spreading. From Fig. 9, there is lateral flow happen to high viscosity melts after long period of dwell time (no less than 100 min) in either APS or EB-PVD samples, which is much slower than that at 1400 °C and 1600 °C.

The schematics describing the principle of spreading and infiltration are depicted in Fig. 9a. It is noted that the bubbles formed between melts and APS coating (Figs. 9b and c) disappeared from the melts after 10^3 min (Figs. 9d and e), whereas no bubbles were formed in the melts on EB-PVD sample (Figs. 9g-j).

To further looking into the mechanisms, we compare the surface (Fig. 6a) and cross section morphologies (Fig. 9) of samples in the transition state (e.g. APS/EB-PVD TBCs sample at 1200 °C with dwell time of 10^3 min). From the Si elemental mapping, the TBCs after melt exposure can be divided into different areas by dashed lines (Figs. 9d and i): (1) melts concentration area, (2) melts fully spread area, and (3) lateral flow area. Among the areas, the melts concentration area and the melts fully-spread area are corresponding to the darker-colored area and the lighter-colored area in Fig. 6a, respectively. There are no observable melts on the corresponding surface of lateral flow area. However, both (2) and (3) can be only identified in the samples exposed to melt for a prolonged period or at very high temperature.

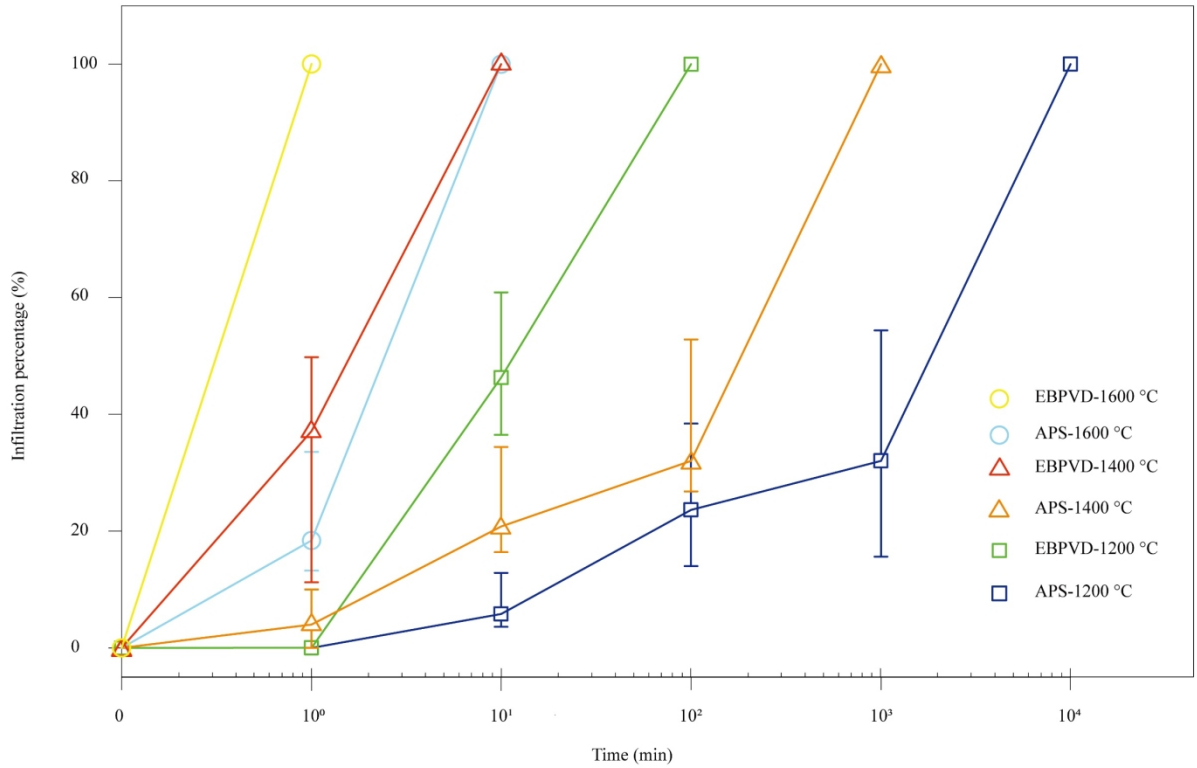

Fig. 8. The average melts infiltration percentage (infiltration depth/ thickness of coating) in each sample assembly. The infiltration percentage are measured every 50 μm along the lateral direction. The error bars indicate minimum and maximum values.

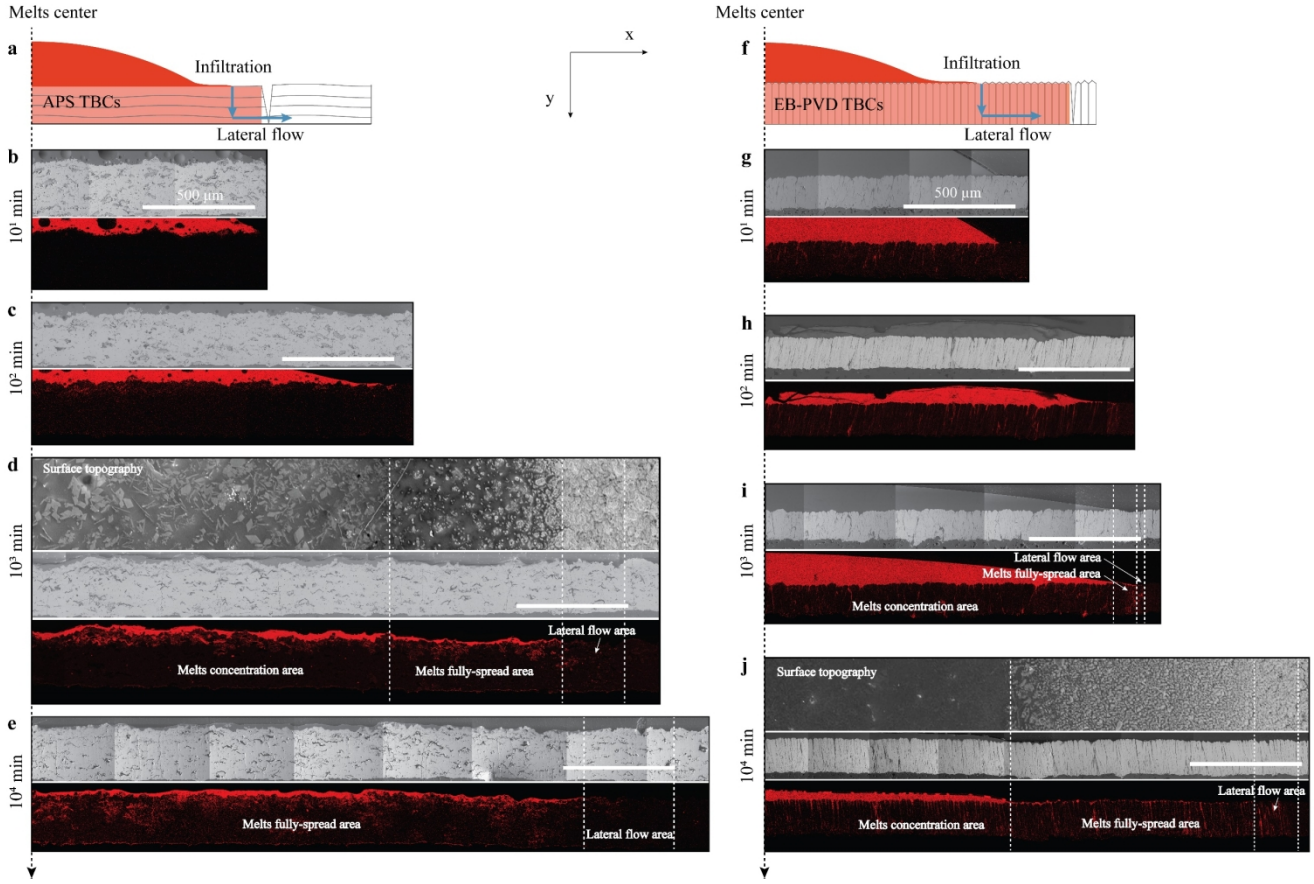

Fig. 9. Schematic, cross-section SEM images and Si elemental mappings of the melt-deposited APS and EB-PVD TBCs samples exposed to 1200 °C for 10^1-10^4 min. (**a**) Schematic cross-section of melt-deposited APS TBC. Cross-section SEM image and Si elemental mapping of the melt-deposited APS TBCs after 10 min (**b**), 10^2 min (**c**), 10^3 min (including a surface morphology image) (**d**) 10^4 min (**e**). (**f**) Schematic cross-section of melt-deposited EB-PVD TBC. Cross-section SEM image and Si elemental mapping of the melt-deposited EB-PVD TBCs after 10 min(**g**), 10^2 min (**h**), 10^3 min (**i**) and 10^4 min (including a surface morphology image and zooming in image of the crack) (**j**). The left edge of each picture is the center of the melts. All the pictures are with the same magnification and could be compared directly. The scales of the merged image are with the length of 500 μm. Vertical dashed lines separate different areas.

As can be seen in Figs. 9e and j, we know that the thin melt film in the melts fully spread area does not cover the peaks of rough TBCs surfaces, which is the reason for the lighter appearance in this area. Such a phenomenon may occur when the rate of melt spreading onto this area is less than the rate of melt loss due to infiltration. From the top view (Fig. 6), both the melt concentration area and the area of total spreading can be observed with the naked eye, but the subsurface lateral flow area could not be observed by surface imaging.

4. Discussion

In this study, the silicate melts initially spread across the surface of the TBCs and then, driven by the capillary forces, infiltrated vertically into the TBCs and flew laterally along the subsurface inter-

column structure of EB-PVD TBCs, or along the lamellar structure in APS TBCs. The rate at which these processes occur was controlled by the melt concentration gradient, the melt viscosity and the anisotropy of the microstructure of the TBCs. In summary, the spreading and infiltration of re-melted volcanic ash melts on different TBCs are controlled by many factors which adopt the leading role alternately under different conditions and in different stages, as illustrated in Fig. 10 and described here.

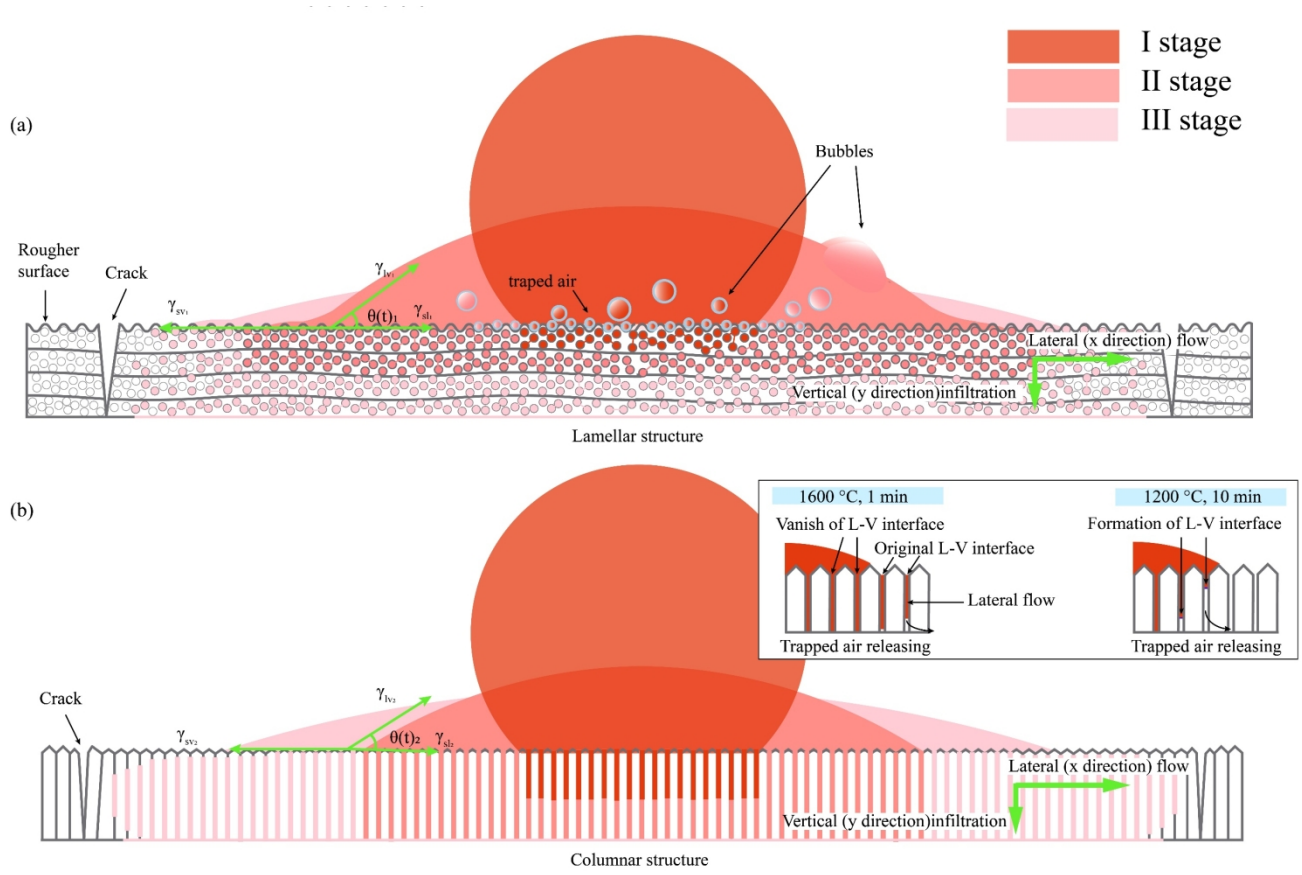

Fig. 10. The schematic of spreading and infiltration of melts on (**a**) APS TBCs and (**b**) EB-PVD TBCs. The insert in Fig. 9b is the schematic of spreading process with/without the existence of lateral flow (L-V interface refers to Liquid-vapor interface).

Stage I: during the short period of spreading in stage I (yellow area, Figs. 6b-d), the driving force of spreading mainly derives from the unbalanced combined force of surface tension ('γ_{sv}-γ_{sl}-γ_{lv}·cosθ' in Fig. 10). The main resistance of spreading originates from melt viscosity. The viscosity of the melts, the physical property governing the flow process, decreases exponentially with temperature.

291 Therefore, the spreading area at higher temperature are larger after the same dwell time due to a lower
292 melt viscosity and more efficient spreading.

293 At the end of stage I, at relatively low target temperatures (inserted into 1200 °C for 10 min and
294 inserted into 1400 °C for 1 min, respectively, see the heating profile of the beads in Fig. S3), the large
295 dynamic contact angle of the melts promotes a high initial spreading rate on both types of coating and
296 the influence of TBCs microstructure can be ignored. In other words, the limited infiltration during
297 this short period of time has limited influence on the spreading process. Thus the extent of the
298 spreading on both types of TBCs are similar at any given temperature, irrespective of absolute
299 temperature is.

300 After inserted into target temperature of 1600 °C, the melt temperature reached 1265 °C at the end of
301 stage I. At this temperature the greatly decreased viscosity yields spreading, infiltration and lateral
302 flow behaviors which are more sensitive to the surface roughness and microstructures of the TBCs.
303 Thus, although the spreading areas on both kinds of TBCs are similar, the infiltration and lateral flow
304 within their microstructures are quite different. From Figs. 7c and d bottom, there is no subsurface
305 lateral flow observed in the APS TBCs within 1 min, whereas for the EB-PVD TBCs the lateral flow
306 of melt rapidly filled the highly connective columnar structure and radially extend far beyond the
307 spreading front on the TBCs surface at 1600 °C (diffusion distance >5.3 mm within 1 min). For the
308 TBCs with lower connected micro-porosity or lower environmental temperature, the lateral flow
309 could also occur but extends more slowly and thus not as far as the former (e.g. after dwell time of
310 10^4 min at 1200 °C, the lateral flow in APS TBCs reached 402 μm compare to lateral flow further
311 than 5260 μm for EB-PVD TBCs at 1600 °C for 1 min).

312 The capillary length of melts was calculated as described in 'Supplementary Calculation: capillary
313 length calculation of Tungurahua volcanic ash melt'. Where it is observed that the effect of gravity on
314 a 1 mm andesite glass bead is negligible during spreading, infiltration and lateral flow. When melts
315 spread over an area which already affected by lateral flow, the spreading melt will contact with the

316 subsurface melt then the loss of the original liquid-vapor interface in this situation causes a decrease
317 of surface energy (inset in Fig. 10b, left). In contrast, the liquid-vapor interface formed between
318 spreading melts and trapped air in the non-lateral flow condition (inset in Fig. 10b, right) results a
319 relatively high surface energy and thus a lower driving force for spreading. In such cases, the surface
320 spreading process might be accelerated with the existence of subsurface lateral flow.

321 We would like to stress that in fact such lateral flow might yield catastrophic consequences to which
322 more attention should be paid in the future. As previously stated [50], molten silicates can penetrate
323 the top protective $La_2(Zr_{0.7}Ce_{0.3})O_7$ layer in the $La_2(Zr_{0.7}Ce_{0.3})O_7$/YSZ coating through the vertical
324 cracks and then may undergo lateral flow along the coating interface. Consequently, subsurface lateral
325 flow could contaminate the entire EB-PVD YSZ coating beyond the regions with vertical cracks,
326 rendering the protective top coating irrelevant. Since the subsurface lateral flow is strongly influenced
327 by temperature, when engine operational temperature increases, the hazard caused by volcanic ash to
328 the engine will be increasingly problematic. Manufacturing twisted gaps between columns might be
329 a solution to avoid rapid lateral flow in EB-PVD TBCs.

330 **Stage II:** when the melts equilibrate to the target temperature (blue area, Figs. 6b-d), the viscosity
331 decreases to values lower than that in stage I (>362 Pa·s at 1200 °C, 80.7 Pa·s at 1400 °C, 10.3 Pa·s
332 at 1600 °C). This increased fluidity of melts promotes an increasingly significant interaction with the
333 rough surface and microstructure of TBCs. Therefore, the microstructure and surface roughness of
334 TBCs become the dominant factor controlling spreading in stage II.

335 The surface spreading and vertical infiltration processes in the TBCs can be viewed as competitive
336 processes. In stage II, the spreading mainly influenced by different infiltration behavior between APS
337 and EB-PVD TBCs. The highly connected columnar microstructure causes the high infiltration
338 velocity of melts in EB-PVD TBCs which will decrease the spreading rate on it compare to APS
339 TBCs. The type of microstructure (the shape and connectivity of pores) determines how rapid the
340 melts can be absorbed into the pores of the TBCs. Thus, the limited infiltration velocity at initial stage

permits faster spreading on APS TBCs, even though the higher curvature of the pores permits greater capillary forces to act upon the melts [30].

On the other hand, for a wetting liquid, a rough surface is a semi-porous medium, which is more easily covered and coated by a liquid than a flat surface due to capillary forces [51−52]. Accordingly, the driving force and wettability of spreading melt on a rougher surface is higher than that on a smooth surface. Indeed, we observe that the APS TBCs, with a rougher surface, are more rapidly wetted than EB-PVD TBCs (Figs. 9 c-d, h-i). It is further observed that the spreading front of lower viscosity melts are more easily influenced by the surface roughness of TBCs, thus their spreading front edge morphologies are not as smooth as those of high viscosity melts.

Additionally, in Stage II, trapped air bubbles form in the melts on the APS TBCs. Bubbles are mainly derived from trapped air in the void space between the melts and the rough surface of the TBCs. The trapped air between the melt and the EB-PVD TBCs is released through the connected pores, while the disconnected pores in APS TBCs prevent air escape, leading to trapped air in the melts. Therefore, the formation of the bubbles is related to the surface morphology and the connectivity of the pores. The bubbles will increase the dynamic contact angle θ (t) (Fig. 10) between the melts and APS TBCs, thus increasing the flowing driving force F_d according to equation (1) [53]:

$$F_d(t) = \gamma_{LV}[cos\theta_E - cos\theta(t)] \qquad (1)$$

where $\theta_E$is the equilibrium contact angle of the melts on YSZ TBCs and spreading rate before the air is completely released from the upper surface of the melt (after 10^3 min). As a result, a polished TBCs surface with lower surface roughness might be suggested to release the hazard of trapped air bubble. As a result, the difference of spreading radius on two type of TBCs in stage II increase with time.

Stage III: only samples at 1200 °C and 1400 °C are considered here due to the spallation of the TBCs at 1600 °C in this stage. Up to this stage, the low-connectivity pores in the APS TBCs have sufficient

time to absorb the melts. The porosity, which is the percentage of the pores and columns, dictates the space available for melt penetration which in turn affects spreading [54]. Thus, the relatively larger porosity in APS TBCs leads to greater amount of melt infiltration into the microstructure, reducing the relative spreading rate compared to the EB-PVD TBCs. Consequently, the spreading rate of melts on EB-PVD TBCs is higher than that on APS TBCs in stage III.

The wetting, spreading and infiltration of molten volcanic ash on TBC are processes that throughout the whole degradation procedure which may greatly dictate the extent of corrosive attack (range and depth of chemical interactions and mechanical damage). The serious corrosion caused by silicate melt can lead to premature spallation of the top coating and further give rise to catastrophic air safety issues.

5. Conclusions

The spreading and infiltration process of melts inflenced by environmental temperature and TBCs structures has been experimentally investigated. Results indicate that the spreading areas, infiltration depths and lateral flow distances increase greatly with temperature due largely to the exponential decrease in melt viscosity. At each environmental temperature, the spreading process can be divided into three stages: (1) in stage I, the spreading areas on APS TBCs and EB-PVD TBCs are similar due to the high driving force for melt spreading and the relatively high melt viscosity; (2) in stage II, the type of microstructure (the shape and connectivity of pores) and surface roughness, which could futher influence the formation of trapped air bubble, play an important role. The spreading rates on APS TBCs are faster than that on EB-PVD TBCs mainly as a result of the higher infiltration rate in EB-PVD TBCs which can decrease the corresponding spreading. The higher surface roughness on APS TBCs, which can increase the wettability of melts, may also play a role in accelerating spreading. Additionally, the trapped air formed between the melts and APS TBCs can also increase the spreading rate. Finally, a polished TBCs surface with lower surface roughness might be suggested to release the hazard of trapped air bubble; (3) in stage III, the spreading area on all TBCs become more similar again because of the higher porosity of APS TBCs which decreases the spreading rate on them at this

stage. The higher connectivity of micro-pores in EB-PVD TBCs enables the rapid vertical infiltration rate and lateral flow rate of melts especially at relatively high temperature (e.g., melt viscosity is ~ 10.3 Pa·s at 1600 °C). The existence of subsurface lateral flow would accelerate the surface spreading process.

Acknowledgements

We are grateful to U. Küppers for providing the volcanic ash material, C. Cimarelli for assistance with SEM analyses, S. Lokachari and D. Müller for discussions. H. Guo acknowledges the support of Nature Science Foundations of China (NSFC) (grant numbers 51590894 and 51425102), the 111 Project (grant number B17002), and National Science and Technology Major Project (grant number 2017-VI-0010-0081). W. Song acknowledge the support of "Freigeist" Fellowship of the VolkswagenStiftung on "Volcanic Ash Deposition in Jet Engines" (VADJEs, No 89705). S. Yang acknowledges the financial support from China Scholarship Council (CSC).

Data availability

The raw data required to reproduce these findings cannot be shared at this time as the data also forms part of an ongoing study.

References

1. J. M. Drexler, A. D. Gledhill, K. Shinoda, A. L. Vasiliev, K. M. Reddy, S. Sampath, N. P. Padture, Jet engine coatings for resisting volcanic ash damage, *Adv. Mater.* 23 (2011) 2419−2424. https://doi.org/10.1002/adma.201004783
2. W. Song, K. U. Hess, D. E. Damby, F. B. Wadsworth, Y. Lavallée, C. Cimarelli, D. B. Dingwell, Fusion characteristics of volcanic ash relevant to aviation hazards, *Geophys. Res. Lett.* 41 (2014) 2326−2333. https://doi.org/10.1002/2013GL059182
3. W. Song, Y. Lavallée, K. U. Hess, U. Küppers, C. Cimarelli, D. B. Dingwell, Volcanic ash melting under conditions relevant to ash turbine interactions, *Nat. Commun.* 7 (2016) 10795. https://doi.org/10.1038/ncomms10795
4. M. Guffanti, T. J. Casadevall, K. Budding, Encounters of aircraft with volcanic ash clouds: a compilation of known incidents, 1953−2009, *U. S. Geological Survey Data Series* 545, v1, 2010. https://doi.org/pubs.usgs.gov/ds/545/
5. R. Gertisser, Eyjafjallajökull volcano causes widespread disruption to European air traffic. *Geol. Today*. 26 (2010) 94−95. https://doi.org/ 10.1111/j.1365−2451.2010.00757.x
6. J. L. Smialek, F. A. Archer, R. G. Garlick, Turbine airfoil degradation in the persian gulf war, *JOM*. 46 (1994) 39−41. https://doi.org/ 10.1007/BF03222663
7. M. Dunn, C. Padova, J. Moller, R. Adams, Performance deterioration of a turbofan and a turbojet engine upon exposure to a dust environment, *J. Eng. Gas. Turbine Power* 109 (1987) 336−343. https://doi.org/10.1115/1.3240045
8. D. B. Dingwell, Y. Lavallée, U. Küppers, Volcanic ash: A primary agent in the earth system, *Phys. Chem. Earth* 45 (2012) 2−4. https://doi.org/10.1016/j.pce.2011.07.007
9. D. Giordano, A. R. Nichols, D. B. Dingwell, Glass transition temperatures of natural hydrous melts: A relationship with shear viscosity and implications for the welding process, *J. Volcanol. Geoth. Res.* 142 (2005) 105−118. https://doi.org/10.1016/j.jvolgeores.2004.10.015
10. S. Kumar, N. P. Padture, Materials in the aircraft industry, in: B. Kaufman, C. Briant (Eds), Metallurgical design and industry, Springer, Cham, 2018, pp. 271−346. https://doi.org/10.1007/978-3-319-93755-7_5
11. U. Küppers, C. Cimarelli, K. U. Hess, J. Taddeucci, F. B. Wadsworth, D. B. Dingwell, The thermal stability of Eyjafjallajökull ash versus turbine ingestion test sands, *J. Appl. Volcano.* 3 (2014) 4. https://doi.org/ 10.1186/2191-5040-3-4
12. N. D. Cardwell, K. A. Thole, S. W. Burd, Investigation of sand blocking within impingement and film-cooling holes, *J. Turbomach.* 132 (2010) 021020. https://doi.org/10.1115/1.3106702
13. A. R. Krause, H. F. Garces, G. Dwivedi, A. L. Ortiz, S. Sampath, N. P. Padture, Calcia-magnesia-alumino-silicate (CMAS)-induced degradation and failure of air plasma sprayed yttria-stabilized zirconia thermal barrier coatings, *Acta Mater*. 105 (2016) 355−366. https://doi.org/10.1016/j.actamat.2015.12.044
14. J. Dean, C. Taltavull, T. W. Clyne, Influence of the composition and viscosity of volcanic ashes on their adhesion within gas turbine aeroengines, *Acta Mater.* 109 (2016) 8−16. https://doi.org/10.1016/j.actamat.2016.02.011
15. W. Song, Y. Lavallée, F. B. Wadsworth, K. U. Hess, D. B. Dingwell, Wetting and spreading of molten volcanic ash in jet engines, *J. Phys. Chem. Lett.* 8 (2017) 1878−1884. https://doi.org/10.1021/acs.jpclett.7b00417
16. N. P. Padture, Advanced structural ceramics in aerospace propulsion, *Nat. Mater.* 15 (2016) 804−809.

https://doi.org/10.1038/nmat4687

17. N. P. Padture, M. Gell, E. H. Jordan, Thermal barrier coatings for gas-turbine engine applications, *Science* 296 (2002) 280−284. https://doi.org/10.1126/science.1068609

18. D. R. Clarke, M. Oechsner, N. P. Padture, Thermal-barrier coatings for more efficient gas-turbine engines, *MRS Bull.* 37 (2012) 891−898. https://doi.org/10.1557/mrs.2012.232

19. R. Darolia, Thermal barrier coatings technology: Critical review, progress update, remaining challenges and prospects, *Int. Mat. Rev.* 58 (2013) 315−348. https://doi.org/10.1179/1743280413Y.0000000019

20. N. P. Padture, Environmental degradation of high-temperature protective coatings for ceramic-matrix composites in gas-turbine engines, *npj Mater. Degrad.* 3 (2019) 11. https://doi.org/10.1038/s41529-019-0075-4

21. H. Zhao, C. G. Levi, H. N. G. Wadley, Molten silicate interactions with thermal barrier coatings, *Surf. Coat. Techol.* 251 (2014) 74−86. https://doi.org/10.1016/j.surfcoat.2014.04.007

22. X. Cao, R. Vassen, D. Stoever, Ceramic materials for thermal barrier coatings, *J. Eur. Ceram. Soc.* 24 (2004) 1−10. https://doi.org/10.1016/S0955-2219(03)00129-8

23. W. Pan, S. R. Phillpot, C. Wan, A. Chernatynskiy, Z. Qu, Low thermal conductivity oxides, *MRS Bull.* 37 (2012) 917−922. https://doi.org/10.1557/mrs.2012.234

24. Y. Tan, J. P. Longtin, S. Sampath, H. Wang, Effect of the starting microstructure on the thermal properties of as-sprayed and thermally exposed plasma-sprayed ysz coatings, *J. Am. Ceram. Soc.* 92 (2009) 710−716. https://doi.org/10.1111/j.1551-2916.2009.02953.x

25. J. M. Drexler, K. Shinoda, A. L. Ortiz, D. Li, A. L. Vasiliev, A. D. Gledhill, S. Sampath, N. P. Padture. Air-plasma-sprayed thermal barrier coatings that are resistant to high-temperature attack by glassy deposits, *Acta Mater.* 58 (2010) 6835−6844. https://doi.org/10.1016/j.actamat.2010.09.013

26. C. G. Levi, J. W. Hutchinson, M. H. Vidal-Sétif, C. A. Johnson, Environmental degradation of thermal-barrier coatings by molten deposits, *MRS Bull.* 37 (2012) 932−941. https://doi.org/10.1557/mrs.2012.230

27. D. Bonn, J. Eggers, J. Indekeu, J. Meunier, E. Rolley, Wetting and spreading, *Rev. Mod. Phys*. 81 (2009) 739−805. https://doi.org/10.1103/RevModPhys.81.739

28. X. Shan, L. Luo, W. Chen, Z. Zou, F. Guo, L. He, A. Zhang, X. Zhao, P. Xiao, Pore filling behavior of YSZ under CMAS attack: Implications for designing corrosion-resistant thermal barrier coatings, *J. Am. Ceram. Soc.* 101 (2018) 5756−5770. https://doi.org/10.1111/jace.15790

29. R. Naraparaju, J. J. G. Chavez, U. Schulz, C. V. Ramana, Interaction and infiltration behavior of Eyjafjallajökull, Sakurajima volcanic ashes and a synthetic CMAS containing FeO with/in EB-PVD ZrO_2-65 wt% Y_2 O_3 coating at high temperature, *Acta Mater.* 136 (2017) 164−180. https://doi.org/10.1016/j.actamat.2017.06.055

30. S. Krämer, J. Yang, C. G. Levi, C. A. Johnson, Thermochemical interaction of thermal barrier coatings with molten CaO-MgO-Al_2O_3-SiO_2 (CMAS) deposits, *J. Am. Ceram. Soc.* 89 (2006), 3167−3175. https://doi.org/10.1111/j.1551-2916.2006.01209.x

31. J. M. Drexler, A. L. Ortiz, N. P. Padture, Composition effects of thermal barrier coating ceramics on their interaction with molten Ca-Mg-Al-silicate (CMAS) glass, *Acta Mater.* 60 (2012) 5437−5447. https://doi.org/10.1016/j.actamat.2012.06.053

32. H. F. Garces, B. S. Senturk, N. P. Padture, In situ raman spectroscopy studies of high-temperature degradation of thermal barrier coatings by molten silicate deposits, *Scr. Mater.* 76 (2014) 29−32. https://doi.org/10.1016/j.scriptamat.2013.12.008

33. X. Zhou, T. Chen, J. Yuan, Z. Deng, H. Zhang, J. Jiang, X. Cao, Failure of plasma sprayed nano-zirconia -based thermal barrier coatings exposed to molten CaO-MgO-Al_2O_3-SiO_2 deposits, *J. Am. Ceram. Soc.* 102 (2019), 6357-6371. https://doi.org/10.1111/jace.16498

34. R. W. Jackson, E. M. Zaleski, D. L. Poerschke, B. T. Hazel, M. R. Begley,C. G. Levi, Interaction of molten silicates with thermal barrier coatings under temperature gradients, *Acta Mater.* 89 (2015) 396−407. https://doi.org/10.1016/j.actamat.2015.01.038

35. X. Zhou, L. He, X. Cao, Z. Xu, R. Mu, J. Sun, J. Yuan, B. Zou, $La_2(Zr_{0.7}Ce_{0.3})_2O_7$ thermal barrier coatings prepared by electron beam-physical vapor deposition that are resistant to high temperature attack by molten silicate, *Corros. Sci.* 115 (2017) 143-151. https://doi.org/10.1016/j.corsci.2016.11.015

36. G. Li, C. Cai, Y. Wang, Y. Zhou, L. Yang, J. Lu, G. Zhou, Zirconium silicate growth induced by the thermochemical interaction of yttria-stablized zirconia coatings with molten CMAS deposits, *Corros. Sci*. 149 (2019) 249-256. https://doi.org/10.1016/j.corsci.2019.01.011

37. C. Mercer, S. Faulhaber, A. G. Evans, R. Darolia, A delamination mechanism for thermal barrier coatings subject to calcium-magnesium-alumino-silicate (CMAS) infiltration, *Acta Mater.* 53 (2005) 1029−1039. https://doi.org/10.1016/j.actamat.2004.11.028

38. B. C. Zhang, K. Chen, N. Baddour, P. C. Patnaik, Failure and life evaluation of EB-PVD thermal barrier coatings using temperature-process-dependent model parameters, *Corros. Sci.* 156 (2019) 1-9. https://doi.org/10.1016/j.corsci.2019.04.020

39. J. M. Drexler, A. Aygun, D. Li, R. Vaßen, T. Steinke, N. P. Padture, Thermal-gradient testing of thermal barrier coatings under simultaneous attack by molten glassy deposits and its mitigation, *Surf. Coat. Technol*. 204 (2010) 2683−2688. https://doi.org/10.1016/j.surfcoat.2010.02.026

40. R. Naraparaju, H. Lau, M. Lange, C. Fischer, D. Kramer, U. Schulz, K. Weber, Integrated testing approach using a customized micro turbine for a volcanic ash and CMAS related degradation study of thermal barrier coatings, *Surf. Coat. Technol.* 337 (2018) 198−208. https://doi.org/ 10.1016/j.surfcoat.2018.01.030

41. S. Krämer, J. Yang, C. G. Levi, Infiltration-inhibiting reaction of gadolinium zirconate thermal barrier coatings with CMAS melts, *J. Am. Ceram. Soc.* 91 (2008) 576−583. https://doi.org/10.1111/j.1551-2916.2007.02175.x

42. W. Chen, L. Zhao, Review-volcanic ash and its influence on aircraft engine components, *Procedia Eng.* 99 (2015) 795−803. https://doi.org/10.1016/j.proeng.2014.12.604

43. J. W. Neuberg, A. S. Collinson, P. A. Mothes, M. C. Ruiz, S. Aguaiza, Understanding cyclic seismicity and ground deformation patterns at volcanoes: Intriguing lessons from tungurahua volcano, ecuador, Earth Planet, *Sci. Lett.* 482 (2018) 193−200. https://doi.org/10.1016/j.epsl.2017.10.050

44. D. B. Dingwell, D. Virgo, The effect of oxidation state on the viscosity of melts in the system Na2O-FeO-Fe2O3-SiO2, *Geochim. Cosmochim. Acta* 51 (1987) 195−205. https://doi.org/10.1016/0016-7037(87)90231-6

45. D. Giordano, J. K. Russell, D. B. Dingwell, Viscosity of magmatic liquids: a model, *Earth Planet Sci. Lett.* 271 (2008) 123−134. https://doi.org/ 10.1016/j.epsl.2008.03.038

46. D. B. Dingwell, S. L. Webb, Relaxation in silicate melts, *Eur. J. Mineral.* 4 (1990) 427−449. https://doi.org/10.1127/ejm/2/4/0427

47. T. Melchior, M. Bläsing, G. Pütz, M. Müller, Surface tension measurements of coal ash slags under reducing conditions at elevated pressures, *Fuel* 90 (2011) 280−287. https://doi.org/10.1016/j.fuel.2010.07.051

48. X. Shan, Z. Zou, L. Gu, L. Yang, F. Guo, X. Zhao, P. Xiao, Buckling failure in air-plasma sprayed thermal barrier coatings induced by molten silicate attack, *Scr. Mater.* 113 (2016) 71−74. https://doi.org/10.1016/j.scriptamat.2015.09.029

49. P. G. De Gennes, F. Brochard-Wyart, D. Quéré, Capillarity and wetting phenomena: drops, Bubbles, pearls, waves, Springer Science & Business Media, Luxemburg, 2004. https://doi.org/10.1007/978-0-387-21656-0

50. X. Zhou, J. Wang, J. Yuan, J. Sun, S. Dong, L. He, X. Cao. Calcium-magnesium-alumino-silicate induced degradation and failure of La_2 $(Zr_{0.7}Ce_{0.3})_2O_7$/YSZ double-ceramic-layer thermal barrier coatings prepared by electron beam-physical vapor deposition. *J. Eur. Ceram. Soc.* 38 (2018) 1897−1907. https://doi.org/10.1016/j.jeurceramsoc.2017.10.057

51. Quéré, D, Rough ideas on wetting, *Physica A*. 313 (2002) 32−46. https://doi.org/10.1016/S0378-4371(02)01033-6

52. R. N. Wenzel, Surface roughness and contact angle, *J. Phys. Chem.* 53 (1949) 1466−1467. https://doi.org/10.1021/j150474a015

549 53. M. Wu, L. Chang, L. Zhang, X. He, X. Qu, Effects of roughness on the wettability of high temperature
550 wetting system, *Surf. Coat. Techol.* 287 (2016) 145-152. https://doi.org/10.1016/j.surfcoat.2015.12.092
551 54. J. G. Li, H. Hausner, Wetting and infiltration of graphite materials by molten silicon, *Scripta Metall. Mater.*
552 32 (1995) 377−382. https://doi.org/10.1016/S0956-716X(99)80068-5

Supplementary Material

Dynamic spreading of re-melted volcanic ash bead on thermal barrier coatings

Shanjie Yang[a,b], Wenjia Song[a,b]*, Yan Lavallee[c], Xin Zhou[b], Donald Bruce Dingwell[b] , Hongbo Guo[a]*

[a] Department of Materials Science and Engineering, Beihang University, Beijing 100191, China.

[b] Department of Earth and Environmental Sciences, Ludwig-Maximilians-Universität München, Theresienstrasse 41, 80333 Munich, Germany.

[c] Department of Earth, Ocean and Ecological Sciences, University of Liverpool, Liverpool L69 3GP, UK

***Corresponding authors**:

Hongbo Guo, Department of Materials Science and Engineering, Beihang University, Beijing 100191, China. (guo.hongbo@buaa.edu.cn)
Telephone: +86 010 82317117

Wenjia Song, Department of Earth and Environmental Sciences, Ludwig-Maximilians-Universität (LMU), Theresienstrasse 41, 80333 Munich, Germany. (wenjia.song@lmu.de)
Telephone: +49 (0) 89 2180 4293

Supplementary Figures and Tables

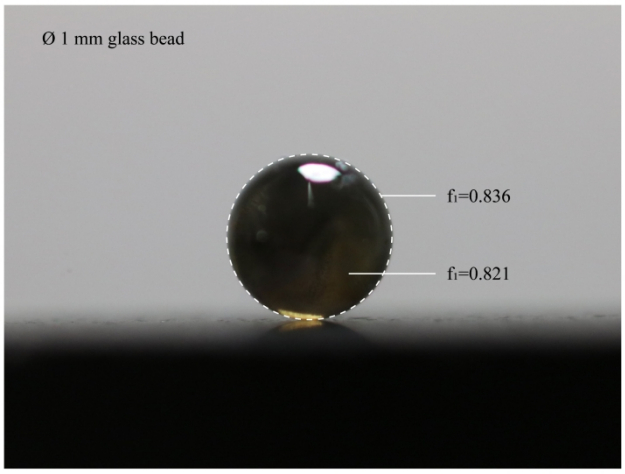

Fig. S1: Measurement of volcanic ash beads. The roundness test of these beads was carried out with the optical dilatometer by comparing the shape factor (f_1) of the glass bead and an ideal sphere. According to the definition of f_1 [1], if the profile of the small drop is in an idea circularity, f_1 amounts to 0.836. The shape factor of the beads measured by optical dilatometer is 0.821-0.860. The high value of the f1 is caused by the baseline automatic positioning error, the real value should be close to the minimum, which is close to that of the ideal sphere. The perfect roundness of the molten drop indicating that: 1) the effect of gravity on the shape formation and spreading/ infiltrating process of the molten drop can be neglected; 2) the equal mass drop has the same shape that is same initial contact angle.

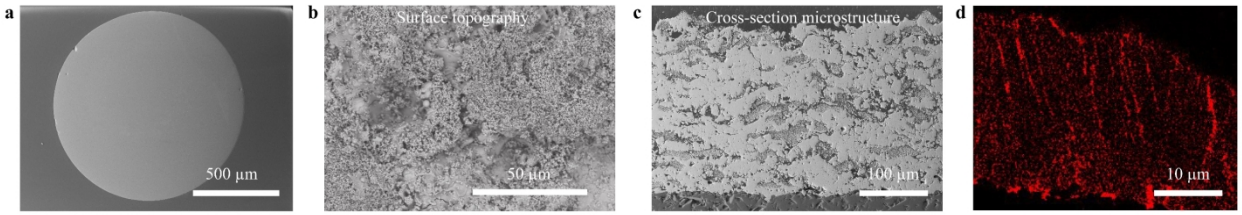

Fig. S2: SEM measurement and EDS analysis. (**a**) Measument of homogenious degree (crystall phase) of the volcanic fagments, beads and melts (Fig. 2c,d below; Fig. 9b right; Fig. 9,10d below) was confirmed using back scattered electron imaging mode to distinguish different phase in the volcanic fragments and beads. Higher density phase backscatter electrons more strongly than that of lower density phase, and thus appear brighter in the image. (**b**) Surface topography image of TBCs (Fig. 4 left; Fig. 8a) and was taken using the secondary electron mode to obtain images with a well-defined, three-dimensional appearance in which the steep surfaces and edges tend to be brighter than flat surfaces. (**c**) Cross section microstructure image of original/infiltrated TBCs (Fig. 4 middle; Fig. 8 inserting image; Fig. 9,10) was taken using back scattered electron imaging mode to detect contrast between areas with different chemical compositions/phase in the glass fragments and beads. heavy elements (higher atomic number) backscatter electrons more strongly than light elements (lower atomic number), and thus appear brighter in the image. (**d**) Si elemental mapping of infiltrated TBCs (Fig. 8, 9,10) was taken with the following parameters: electron acceleration voltage 20 kV, spot intensity 70, energy range 20keV, number of channels 2048, pixel dwell time 30 µs, frame live time 1.5 mins.

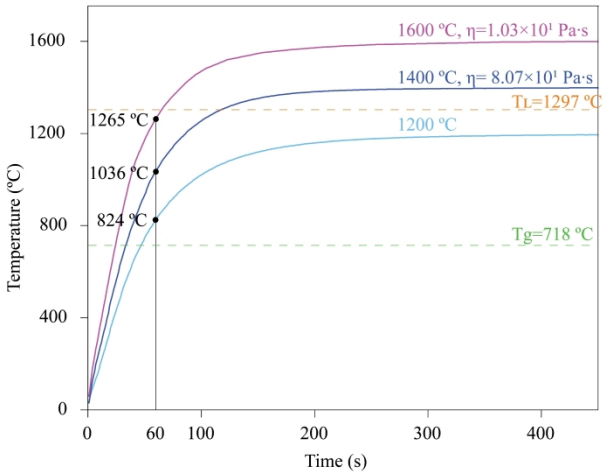

Fig. S3: The heating profile of the sample assembly inserted into the target temperature of 1200 ℃, 1400 ℃ and 1600℃. The temperature of beads inserted into different target temperature for 1 min are marked with orange dot.

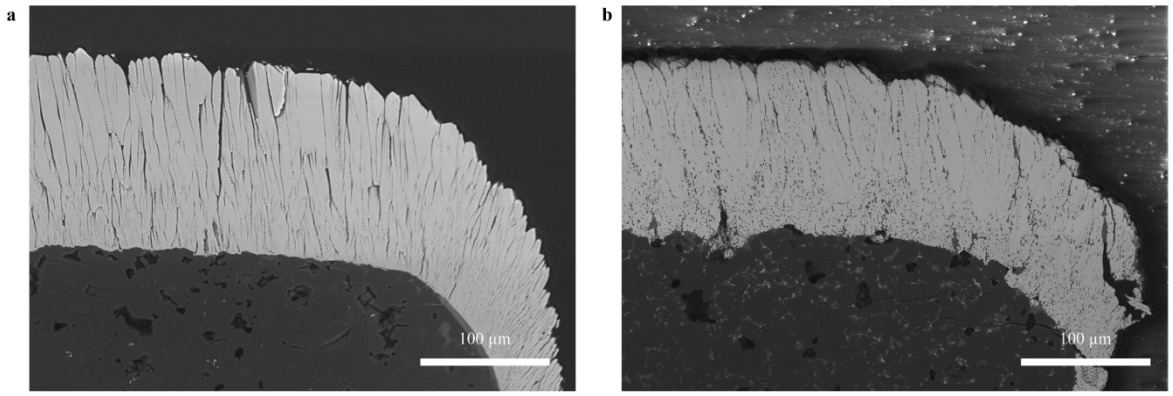

Fig. S4: SEM image at the edge of the EB-PVD TBCs after exposure to 1600 ℃ for 1 min. (**a**) EB-PVD TBCs without melt on the surface; (**b**) EB-PVD TBCs with melt lateral flow at the edge.

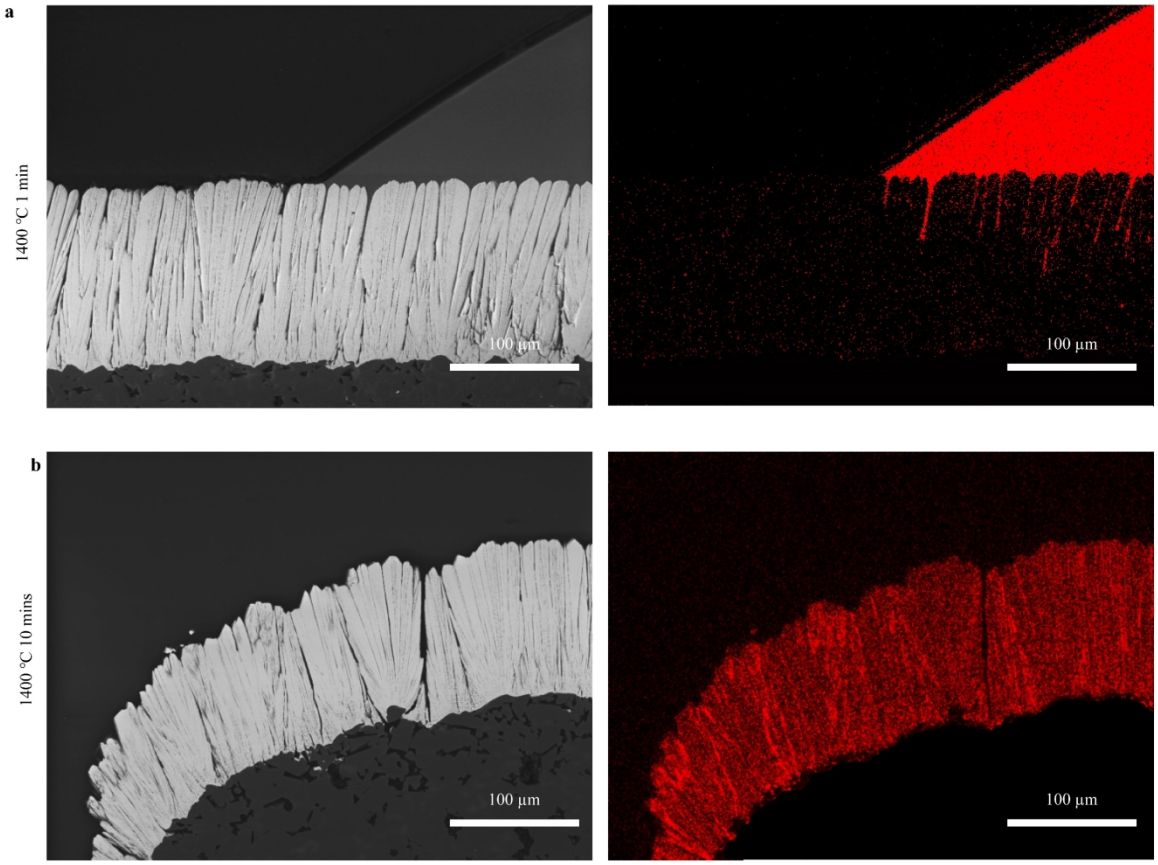

Fig. S5: SEM cross-section image and Si elemental mapping at the edge of the EB-PVD TBC after expose to 1400 ℃ for (**a**) 1 min and (**b**) 10 mins.

Table S1 The viscosity data of Tungurahua volcanic ash at the equilibrium condition.

Temperature (℃)	Viscosity (Pa·s)	Temperature (℃)	Viscosity (Pa·s)
1297	362	1468	46
1321	260	1493	36
1346	194	1517	28
1370	143	1542	22
1395	105	1566	18
1419	79	1590	14
1444	60	-	-

Table S2 The average spreading radii of each sample assembly.

TBCs	Temperature (°C)	Time (min)				
		10^0	10^1	10^2	10^3	10^4
APS	1200	0 mm	1.0 mm	1.6 mm	2.4 mm	2.6 mm
	1400	1.1 mm	2.0 mm	3.3 mm	3.3 mm	-
	1600	1.7 mm	3.3 mm	-	-	-
EB-PVD	1200	0 mm	1.0 mm	1.5 mm	1.7 mm	2.4 mm
	1400	1.0 mm	1.7 mm	2.0 mm	2.6 mm	-
	1600	1.7 mm	2.3 mm	-	-	-

Supplementary Method

Viscosity measurement of Tungurahua volcanic ash

Viscosity measurement was performed using a vertical tube furnace heated by MoSi2 elements, a cylindrical $Pt_{80}Rh_{20}$ crucible (5.1 cm height, 2.56 cm inner diameter, 0.1 cm wail thickness) and a Brookfield RVTD viscometer head. This viscometer head drives a spindle at a range of constant angular velocities (0.5 to 100 rpm) and digitally records the torque exerted on the spindle by the sample. The $Pt_{80}Rh_{20}$ spindle used in this study has the cross-section of a cylinder (1.44 cm diameter, 3.32 cm length) with 45º conical ends to reduce end effects and a 0.24 cm diameter stem. The spindle and head were calibrated for viscosity measurements with the DGG1 standard glass for which the viscosity-temperature relationship is accurately known. The sample had been molten at 1600 ℃ and stiring with a spindle for 24 hours for homogenise and degassing before viscosity measument. Viscosity for the melts was measured at 1 atm and temperatures from 1297 °C to 1590 ℃ in steps of about 25° with the concentric cylinder method. The rotation speed used in the determinations was 50 or 100 rpm. In each temperature step, the melt was continuously stirred for 1h to ensure equilibrated to a time invariance of the viscometer reading as monitored by the chart recorder and the final viscosity determination was obtained. The maximum imprecision is ±3%.

Supplementary Calculation

capillary length calculation of Tungurahua volcanic ash melt

In fluid mechanics, capillary length (κ^{-1}) is a characteristic length scale for an interface between two fluids which is subject both to gravitational acceleration and to a interface force due to surface tension. When the radius of a small drop is less than the capillary length, the effect of gravity is negligible, and the capillary forces become dominant. In this study, the lowest κ^{-1} value for andesite melts was estimated from the following expression [1].

$$\kappa^{-1} = \sqrt{\frac{\gamma}{\rho g}} \qquad (2)$$

where γ, ρ and g are surface tension, density of the drop and gravitational acceleration (g=9.8 m/ s^2), respectively. Accroding to refrence [2], γ ranges from 0.34-0.42 N m^{-1} at 1200-1500 ℃. To estimate the κ^{-1}, conservative value 0.34 N m^{-1} was used here to aquire the lowest κ^{-1}. Besides, density of ρ=2781kg/m^3 at room temperature was adopted because the volume of the melts increase with the experimental temperature thus decrease the drop density. For most silicate glasses, the change of surface tension with temperature is less than 10%. The influence of composition on the surface tension of silicate glass melts is not significant [3], and we can therefore provide a conservative estimate of surface tension as (100%-10%)×0.34 =0.306 N m^{-1}. It is important to note that using the lowest surface tension and the density for the glass at room

temperature is conservative, and therefore underestimates the κ^{-1} value. According to equation (2), the most conservative estimate of capillary length is 3.35 mm (13.41 mg), which is larger than the melt droplet used in this study (Φ1 mm, 1.456 mg). The glass beads approximate a perfect sphere, with roundness factor deviating less than 3% from the ideal. Therefore, the main driving force during spreading, infiltration and lateral flow is the combination of surface tension and capillary forces. The molten sphere will become a sessile drop which takes the shape of a spherical cap, following the solution of the Young-Laplace equation when gravity can be neglected.

Reference

1. P. G. De Gennes, F. Brochard-Wyart, D. Quéré, Capillarity and wetting phenomena: drops, Bubbles, pearls, waves, *Springer Science & Business Media*, Luxemburg, 2004. https://doi.org/10.1007/978-0-387-21656-0
2. A. R. McBirney, T. Murase, Factors governing the formation of pyroclastic rocks, *Bull. Volcanol.* 34 (1970) 372-384. https://doi.org/10.1007/BF02596762
3. N. P. Bansal, R. H. Doremus, Handbook of glass properties, *Elsevier*, Amsterdam, 2013.